Bio-inspired synthesis and profiling of a potent antiviral flavonol targeting the lipid exchanger OSBP

Gwenaëlle Jézéquel, Zoé Grimanelli, Carole Guimard, Joëlle Bigay, Juliano Haddad, Jérôme Bignon, Cécile Apel, Vincent Steinmetz, Laurie Askenatzis, Hélène Levaïque, et al.

▶ To cite this version:

Gwenaëlle Jézéquel, Zoé Grimanelli, Carole Guimard, Joëlle Bigay, Juliano Haddad, et al.. Bio-inspired synthesis and profiling of a potent antiviral flavonol targeting the lipid exchanger OSBP. 2024. hal-04513014

HAL Id: hal-04513014
https://hal.univ-reunion.fr/hal-04513014

Preprint submitted on 20 Mar 2024

Bio-inspired synthesis and profiling of a potent antiviral flavonol targeting the lipid exchanger OSBP

Gwenaëlle Jézéquel[1], Zoé Grimanelli[2], Carole Guimard[1], Joëlle Bigay[2], Juliano Haddad[3], Jérôme Bignon[1], Cécile Apel[1], Vincent Steinmetz[1], Laurie Askenatzis[1], Hélène Levaïque[1], Clara Pradelli[2], Van Cuong Pham[4], Thi May Huong Doan[4], Marc Litaudon[1], Romain Gautier[2], Chaker El Kalamouni[3], Bruno Antonny[2], Sandy Desrat[1], Bruno Mesmin[2*], Fanny Roussi[1*]

[1] Université Paris-Saclay, CNRS, Institut de Chimie des Substances Naturelles, Gif-sur-Yvette, France

[2] Université Côte d'Azur, Inserm, CNRS, Institut de Pharmacologie Moléculaire et Cellulaire, Valbonne, France

[3] Université de la Réunion, INSERM U1187, CNRS UMR 9192, IRD UMR 249, Unité Mixte Processus Infectieux en Milieu Insulaire Tropical, Plateforme Technologique CYROI, 94791 Sainte Clotilde, France

[4] Institute of Marine Biochemistry, Vietnam Academy of Science and Technology, 18 Hoang Quoc Viet, Caugiay, 10000 Hanoi, Vietnam

* Corresponding authors: fanny.roussi@cnrs.fr ; mesmin@ipmc.cnrs.fr

Abstract

Hijacking host cell lipid homeostatic pathways is a hallmark of infection by RNA-positive viruses. A key protein exploited by these viruses to facilitate replication is the lipid exchanger Oxysterol-binding protein (OSBP), making it an attractive target for antiviral strategies. However, the known OSBP ligands are poorly selective, and those of natural origin, referred to as ORPphilins, exhibit pronounced cytotoxicity. Here, we describe macarangin B, a new racemic flavonoid isolated from a Vietnamese bushy tree. This compound features a rare hydroxy-hexahydroxanthene moiety that confers the ability to bind OSBP. Using a bio-inspired method, we performed the total synthesis of both (*R*, *R*, *R*) and (*S*, *S*, *S*) enantiomers, allowing us to examine their distinct interaction with OSBP, based on their unique optical properties. Together, experimental and computational approaches indicate that the (*R*, *R*, *R*) enantiomer has the highest affinity for OSBP. We show that replication of the health-threatening *Flavivirus* Zika virus in infected human cells is strongly reduced by treatment with (*R*, *R*, *R*)-macarangin B, which selectively targets OSBP. Importantly, both enantiomers exhibit significantly decreased cytotoxicity when compared to the previously characterized ORPphilins, positioning (*R*, *R*, *R*)-macarangin B as a promising lead for the development of a novel family of antivirals.

Introduction

Living organisms like plants, marine or micro-organisms produce specialized metabolites to defend themselves against predators or pests. These molecules are designed to kill their attackers by binding to specific protein targets to interfere with metabolic processes. They display precise biological activities due to the optimization of their interaction with their target, which allowed species to survive over the millennia. In this respect, most specialized metabolites are considered to have potential therapeutic utility by binding directly either to the target for which they are designed (*e.g.*, antibiotics) or to a human target showing similarity to the original one [1,2]. According to Waldmann and co-workers, these specialized metabolites can be viewed as privileged structures pre-validated by Nature [3]. They often have highly complex structures with numerous asymmetric centers, which confer them pharmacological specificities. They also display high chemical diversity and embrace a biologically relevant chemical space [4]. However, their structural originality is also their Achilles heel: they are often difficult to synthesize at a multigram scale and their supply can be problematic. Nevertheless, they constitute interesting hits for drug discovery.

In this context, four families of natural molecules with high structural complexity and lacking obvious similarity, produced either by marine organisms (cephalostatin-I [5], ritterazin B [6] and stelletin-E [7]) or plants (OSW-1 [8] and schweinfurthins [9–15]), were described to induce a similar pattern of toxicity against the NCI 60 cancer cell lines (Fig. 1). The COMPARE algorithm predicted these specialized metabolites to have a related mechanism of action, different to that of any of the chemotherapeutics already on the market [16]. Burgett *et al.* showed that these metabolites bind to Oxysterol-binding protein (OSBP) and, to some extent, to its close homolog OSBP-related protein 4 (ORP4) and were thus named ORPphilins [17].

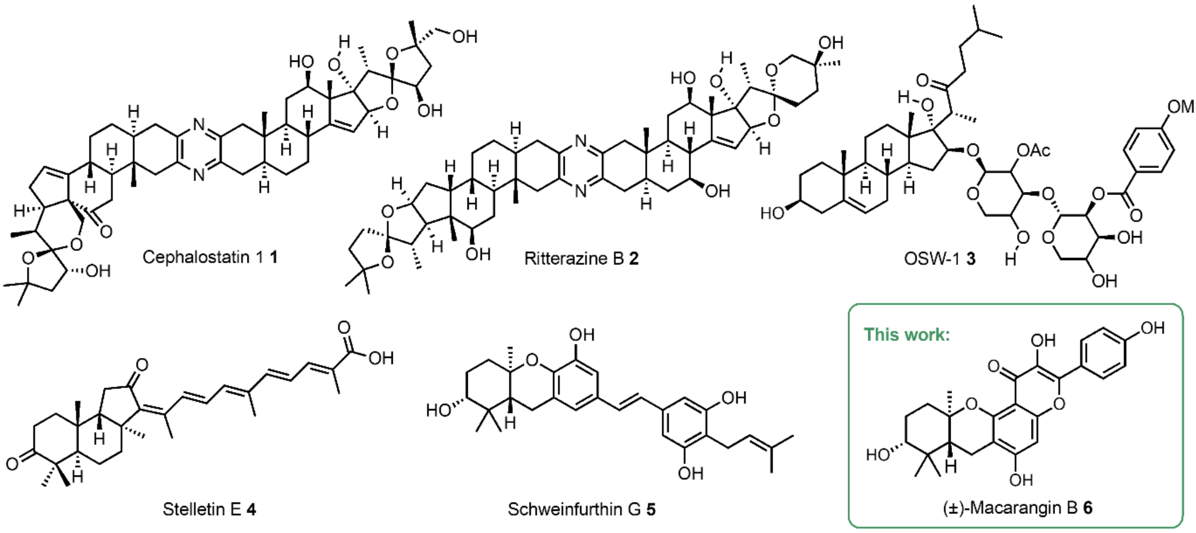

Figure 1. Natural molecules from the ORPphilin family targeting OSBP.

OSBP/ORPs constitute a large and conserved family of intracellular lipid transfer proteins that mainly operate at regions of close apposition between organelles, referred to as membrane contact sites (MCSs) [18]. They all contain a conserved OSBP-related domain (ORD) with a hydrophobic cavity, structured by a near-complete β-barrel fold, which stabilizes sterols and/or non-sterol lipid ligands and enables their transport between membranes [19]. In previous studies, we showed that OSBP transfers cholesterol from the endoplasmic reticulum (ER) to the trans-Golgi network (TGN) by counter exchange and hydrolysis of phosphatidylinositol-4-phosphate [PI(4)P] [20,21], and that OSW-1 **4** or schweinfurthin G (SW-G) **5** inhibit this activity by binding directly within the ORD domain of OSBP [22,23].

Although ORPphilins have been described as promising anticancer agents, the causal relationship between their affinity for OSBP and their cytotoxicity remains elusive, as the role played by this protein in cell survival is still unclear or may be indirect [24,25]. By contrast, evidence suggests that OSBP inhibitors may help combat viral infection since the OSBP machinery is hijacked by many positive-strand RNA viruses [26–31], including the medically relevant dengue and Zika viruses from the *Flavivirus* family, for which no antivirals exist. However, all ORPphilins described so far are highly cytotoxic, compromising their use as potential antiviral drugs. In addition, they all have been isolated in small quantities and their total syntheses are long and complex [32–34]. For example, schweinfurthin (SW) derivatives, which are structurally the "simplest" ORPphilins, require 16 to 20 steps for their synthesis [35].

Here, we isolated a racemic new flavonoid molecule named macarangin B **6** with uncommon hydroxy-HHX moiety from *Macaranga tanarius*, an endemic plant species from Vietnam of the Euphorbiaceae family. We determined that compound **6** is a new ligand of OSBP and inhibits its sterol transfer activity in a dose-dependent manner. We performed the total synthesis of both enantiomers of naturally racemic macarangin B **6**, enabling us to dissect, owing to their optical properties, their specific interaction with OSBP using biochemical and cellular approaches. We further defined the essential OSBP residues responsible for binding macarangin B **6** enantiomers in the ORD cavity by coupling molecular dynamics (MD) simulations to cellular analysis of OSBP mutants. Finally, we showed that Zika virus (ZIKV) replication in infected cells was significantly reduced upon selectively inhibiting OSBP by treatment with macarangin B **6**. Importantly, we provide evidence that both macarangin B **6** enantiomers are much less cytotoxic than other ORPphilins described so far, paving the way for promising new applications as antiviral molecules.

Results

Isolation of macarangin B 6

Macaranga is a large tropical genus of the Euphorbiaceae family, of which 21 species originating from New Caledonia, Madagascar, Uganda and Vietnam are part of an in-house plant collection. A few years ago, we reported the isolation, from *Macaranga tanarius*, of new cytotoxic SW derivatives using molecular networking and mass spectrometry imaging approaches [15,36]. In the isolation process, an original flavonol **6** possessing a similar HHX unit as SW-G was also identified (Fig. 1 and Supporting Information). This compound was isolated at 2 mg scale with a very low extraction yield (0.00017%).

Flavonoids represent one of the most studied classes of specialized metabolites produced throughout the plant kingdom. Their biosynthesis is well-defined and largely conserved [37].

Among them, about 1000 prenylated flavonoids have been isolated but only in 37 plant genera and always in small amounts. They are regarded as phytoalexins and their prenylated structure gives them enhanced biological properties [38,39]. Alkyl chains, mainly prenyl (3,3-dimethylallyl) but also geranyl and farnesyl, are grafted either on cycle A or B of the flavone. The chemical diversity of these metabolites is additionally increased by oxidations, cyclizations with *ortho*-phenolic hydroxyl to form a six-membered pyran derivative, dehydrations or reductions of the prenyl chain. Nevertheless, the hydroxylated *trans*-HHX unit found in compound **6** has never been described so far. However, various prenylated flavones have already been isolated in *Macaranga* species and some molecules of the ugonins family with a *cis*-HHX unit from the rhizomes of *Helminthostachys zeylanica* [40,41].

From a biogenetic point of view, the hydroxy-HHX moiety arises from the intramolecular "head-to-tail" polyene cyclization of a phenol on an epoxidized geranyl side chain [42]. This highly efficient reaction is one of the finest means used by Nature to create complex polycyclic molecules from acyclic ones *via* concerted and stereocontrolled C–C bond formations. In 1955, Eschenmoser and Stork independently rationalized the stereoelectronic aspects that originate the observed stereochemistry in this reaction [43,44]: *trans*-decalins arise from the cyclization of *E*-polyenes, and *cis*-decalins from *Z*-polyenes. Thus, the plausible biosynthetic precursor of compound **6** is (*E*)-macarangin **6**, already isolated from *Macaranga vedeliania* [45] (Fig. 2A). Unlike all SW derivatives with a hydroxy-HHX motif described so far, compound **6** was isolated as a racemate (specific rotation and ECD in Supporting Information), suggesting a non-enzymatic epoxidation of the geranyl chain of macarangin **7**. By contrast, the intramolecular cyclization of the geranyl chain of compound **8** is probably enzymatic as it occurred from the less reactive phenol involved in a hydrogen bond with the adjacent ketone.

The presence of a *trans*-HHX motif similar to that of SW derivatives prompted us to examine whether macarangin B **6** inhibits the cholesterol transfer activity of OSBP. For this, we monitored the transfer of the cholesterol fluorescent analog dehydroergosterol (DHE) by OSBP ORD (residues 401–807) from liposomes mimicking the ER to liposomes mimicking the TGN (Fig.

2B). As previously observed with other ORPphilins [22,23], the DHE transfer rate decreased drastically as we increased the concentration of macarangin B **6** in the reaction mixture (Fig. 2C, D), suggesting that it binds to the ORD domain of OSBP with a high affinity.

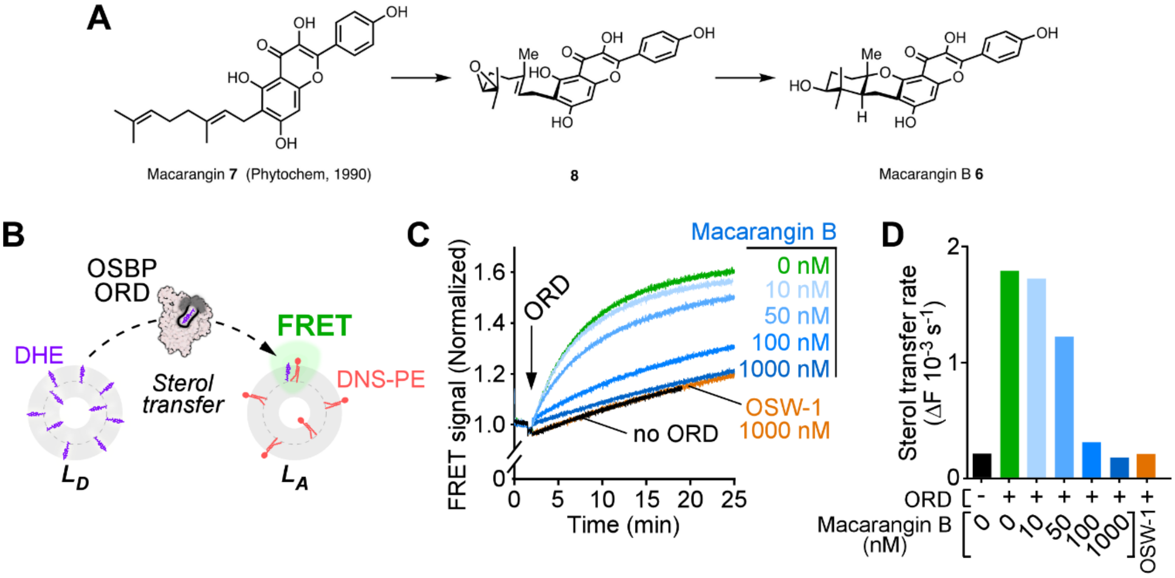

Figure 2. Macarangin B is a new natural OSBP inhibitor. **A.** Biogenetic proposal for macarangin B **6**. **B.** Principle of the sterol transfer assay between donor (*L_D*) and acceptor (*L_A*) liposomes catalyzed by the OSBP ORD domain, as measured by FRET between DHE and DNS-PE. **C.** Time course of DHE transfer between liposomes with increasing amounts Macarangin B **6**, or as a comparison, with OSW-1 (1 µM, orange curve), another OSBP inhibitor. Transfer was initiated by the addition of 100 nM ORD. **D.** Macarangin B **6** inhibits DHE transfer activity in a dose dependent manner.

Bio-inspired synthesis of both enantiomers of macarangin B (*R*)-6 and (*S*)-6

It was previously shown that unnatural (*S*, *S*, *S*) enantiomers of SW derivatives show a distinctive pattern of activity on the NCI 60 cell lines panel compared to their natural (*R*, *R*, *R*) counterparts [48], suggesting that the two-enantiomer series may differ in their mechanisms of action. To verify this hypothesis and because the racemate was isolated with a poor yield and at a small scale, we sought to carry out the synthesis of both (*R*, *R*, *R*) and (*S*, *S*, *S*) enantiomers of macarangin B **6**, *i.e.*, (*R*)-**6** and (*S*)-**6** respectively (Fig. 3). Conventional strategies for synthesizing complex flavonoids are generally based on specific functionalizations on the phenolic moiety before the formation of flavonoid cores. This overcomes the lack of regioselectivity of flavone functionalization, as well as the stability and solubility problems that are sometimes encountered. For example, macarangin **7** has been synthesized in six steps with an overall yield of 6% from benzoyloxyphloroacetophenone, which was alkylated with geranyl bromide before Baker-Venkataraman rearrangement and acid treatment to elaborate the flavone motif [47]. However, to further reduce the number of steps, we performed the bio-inspired synthesis of macarangin B **6** starting from commercial kaempferol **9**, its probable biogenetic precursor.

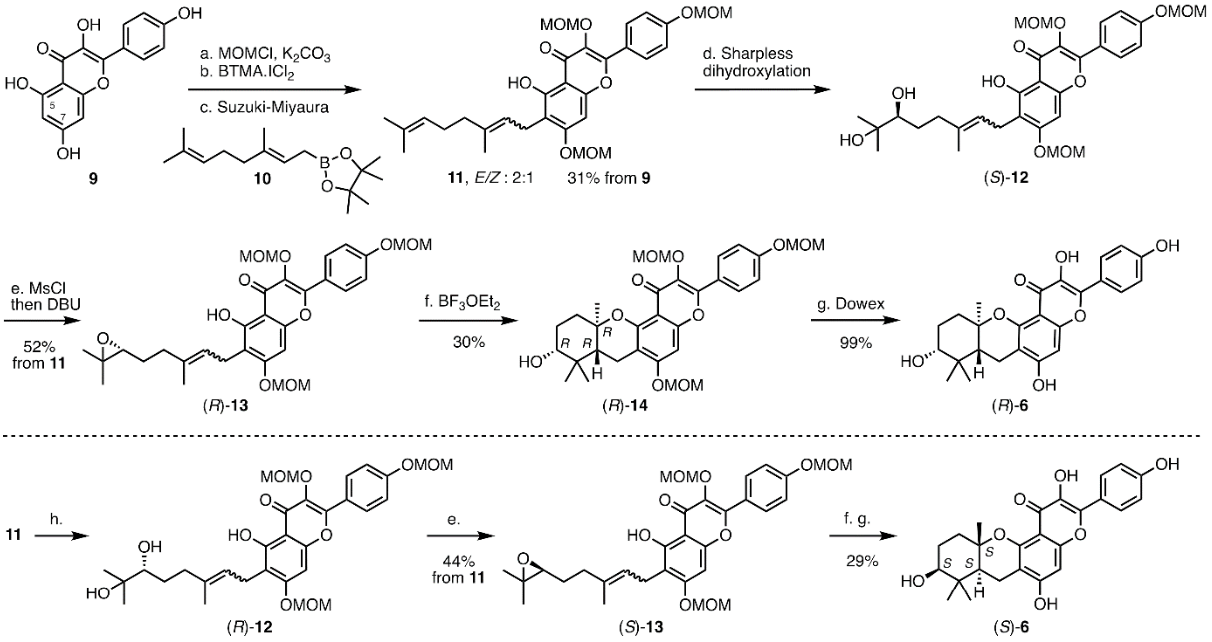

Figure 3. Bio-inspired enantioselective synthesis of macarangin B (*R*)-**6** and (*S*)-**6** in seven steps from kaempferol **9**. Reaction conditions : a. K_2CO_3 (12.0 equiv.), MeCN/DMSO 10:1, 40 °C, 1 h, then dropwise addition (1 h) of MOMCl (5.0 equiv.), room temperature (r.t.), 16 h; b. $NaHCO_3$ (5.0 equiv.), BTMA·ICl_2 (1.05 equiv.), CH_2Cl_2/MeOH 2:1, dark, r.t., 1 h; c. boronic ester **10** (1.5 equiv.), NaOH (2.5 equiv.), $Pd(PPh_3)_4$ (2 mol%), degassed THF/water 2:1, microwave irradiation, 100 °C, 4 h; d. K_2CO_3 (4.0 equiv.), K_3FeCN_6 (2.8 equiv.), $(DHQ)_2PHAL$ (4 mol%), OsO_4 (4 mol%) $MeSO_2NH_2$ (1.3 equiv.), *t*-BuOH/water 2:1, 0 °C, 16 h; e. Et_3N (4.0 equiv.), $MeSO_2Cl$ (2.0 equiv.), r.t., 1 h, then DBU (5.0 equiv.), 0 °C, 3 h; f. BF_3·OEt_2 (1.5 equiv.), CH_2Cl_2, -78 °C, 30 min; g. Dowex 50WX8 200-400 (15.0 equiv.), MeOH, 35 °C, 22 h; h. same as d. but $(DHQD)_2PHAL$ instead of $(DHQ)_2PHAL$.

The direct regioselective introduction of a geranyl chain on the C_6 position of flavonol **9** was first considered. As described previously, the *ortho* position of a phenolate can be alkylated with prenyl bromide, albeit often with low regioselectivity when several phenols are present. The procedures of Baron [48] and Urones [49] (*i.e.*, tetraethylammonium iodide in methanol and aqueous tetramethylammonium hydroxide) did not lead to the *C*-alkylation of kaempferol **9**. The use of other bases (DBU [49], NaH, K_2CO_3 or Et_3N) or solvents (THF, toluene, acetone or TFE) led mainly to the formation of O_7 or C_8 geranylated compounds, revealing that direct C_6 alkylation of flavonol **9** would not be possible with reasonable yields.

Another strategy, based on a Suzuki-Miyaura coupling reaction, was then envisaged to introduce the geranyl chain (Fig. 3). For that, the phenol functions of kaempferol **9** were first protected as methoxymethyl acetal, except the poorly reactive phenol on C_5 engaged in an intramolecular hydrogen bond with the carbonyl moiety. This free phenol was then used to direct regioselective iodination on C_6 in the presence of benzyltrimethylammonium dichloroiodate (BTMA.ICl_2) [51,52]. The iodinated intermediate was obtained with a good regioselectivity of 7:1 in favor of the functionalization of C_6 *versus* C_8 position. The next step consisted in introducing the geranyl chain by a Suzuki-Miyaura coupling using geranyl boronic acid pinacol ester **10** [53]. The choice of appropriate solvents and base turned out to be crucial. The optimal conditions finally involved the use of $Pd(PPh_3)_4$ as a catalyst along with NaOH as a base in a mixture of THF/water 1:1 at 100 °C under microwave irradiation for 4 h. With these conditions, the desired coupling product **11** was obtained in 60% yield over two steps and in 31% yield from kaempferol **9**. However, this reaction was accompanied by partial isomerization of the *E* allylic double bond (*E/Z* 2:1). None of the tested catalysts or conditions could prevent or reduce this side reaction.

When performing direct enantioselective epoxidation of the terminal double bond of compound **11** following Shi or Jacobsen strategies, we observed a lack of chiral induction, regioselectivity and/or very low yield. The desired epoxides (*R*)-**13** and (*S*)-**13** were thus prepared by dihydroxylation followed by cyclization. First, a Sharpless dihydroxylation was carried out in the presence of $(DHQ)_2$PHAL or $(DHQD)_2$PHAL to afford (*S*)-**12** and (*R*)-**12,** respectively. After mesylation of the secondary alcohol obtained, the use of DBU afforded the desired epoxides (*R*)-**13** and (*S*)-**13** with 52% and 44% yield, respectively from geranyl intermediate **11**. The hydroxy-HHX moiety was then obtained by a cascade cyclization induced by a Lewis acid. The use of a stochiometric amount of $BF_3{\cdot}OEt_2$ in dichloromethane at -78 °C afforded the cyclized compounds (*R*, *R*, *R*)-**14**, *i.e.* (*R*)-**14** and (*S*, *S*, *S*)-**14**, *i.e.* (*S*)-**14.** Both could be easily separated from their respective diastereomers arising from the cyclization of (*R*,*Z*)-**13** and (S,*Z*)-

13 (see Supporting Information). The two enantiomers of protected macarangin B (*R*)-**14** and (*S*)-**14** were obtained with good enantiomeric *ratios* (*e.r.*) of 90:10 and 97:3, respectively (see Supporting Information). Gentle deprotection of the phenols using Dowex acidic resin 50WX8 200-400 in methanol at 35 °C for 22 h yielded the two enantiomers of macarangin B (*R*)-**6** and (*S*)-**6** quantitatively. By contrast, classical deprotection with 2 M HCl or *p*-toluenesulfonic acid led to complete degradation. Spectroscopic data (^{1}H and ^{13}C NMR) and mass spectra of (*R*)-**6** and (*S*)-**6** were identical to those of isolated natural macarangin B **6**.

Intrinsic fluorescence of macarangin B (*R*)-6 and (*S*)-6 reveals their enantioselective binding to OSBP

Similarly to 3-hydroxy-flavones, which are known as green or yellow fluorescent metabolites [54-56], natural macarangin B **6** exhibits intrinsic fluorescence with excitation and emission spectra in the UV-visible range (Fig. S1A,B), with two excitation peaks at 280 and 370 nm and two emission peaks at 475 and 550 nm. Interestingly, spectral data analysis revealed high sensitivity to the environment. First, we observed a change in the maximal wavelength and intensity of emission depending on the solvent used (Fig. 4A, S1D). A switch from a polar solvent (methanol, orange curves) to an aqueous medium (black curves) resulted in a red shift with a complete disappearance of the emission peak at 475 nm and a further increase of the emission peak at 550 nm. Second, the addition of detergent micelles (Thesit®) or phosphatidylcholine (PC) liposomes to the aqueous buffer increased the fluorescence signal. Last, upon the addition of the ORD construct of OSBP, the emission peak at 550 nm strongly increased in the case of (*S*)-**6** (Fig. S1D) and even doubled for (*R*)-**6** (Fig. 4A, right panel, blue curve), suggesting the insertion of both compounds within the ORD. These experiments were performed in the presence of PC liposomes to facilitate ligand exchange within the ORD, which was purified with bound cholesterol [23].

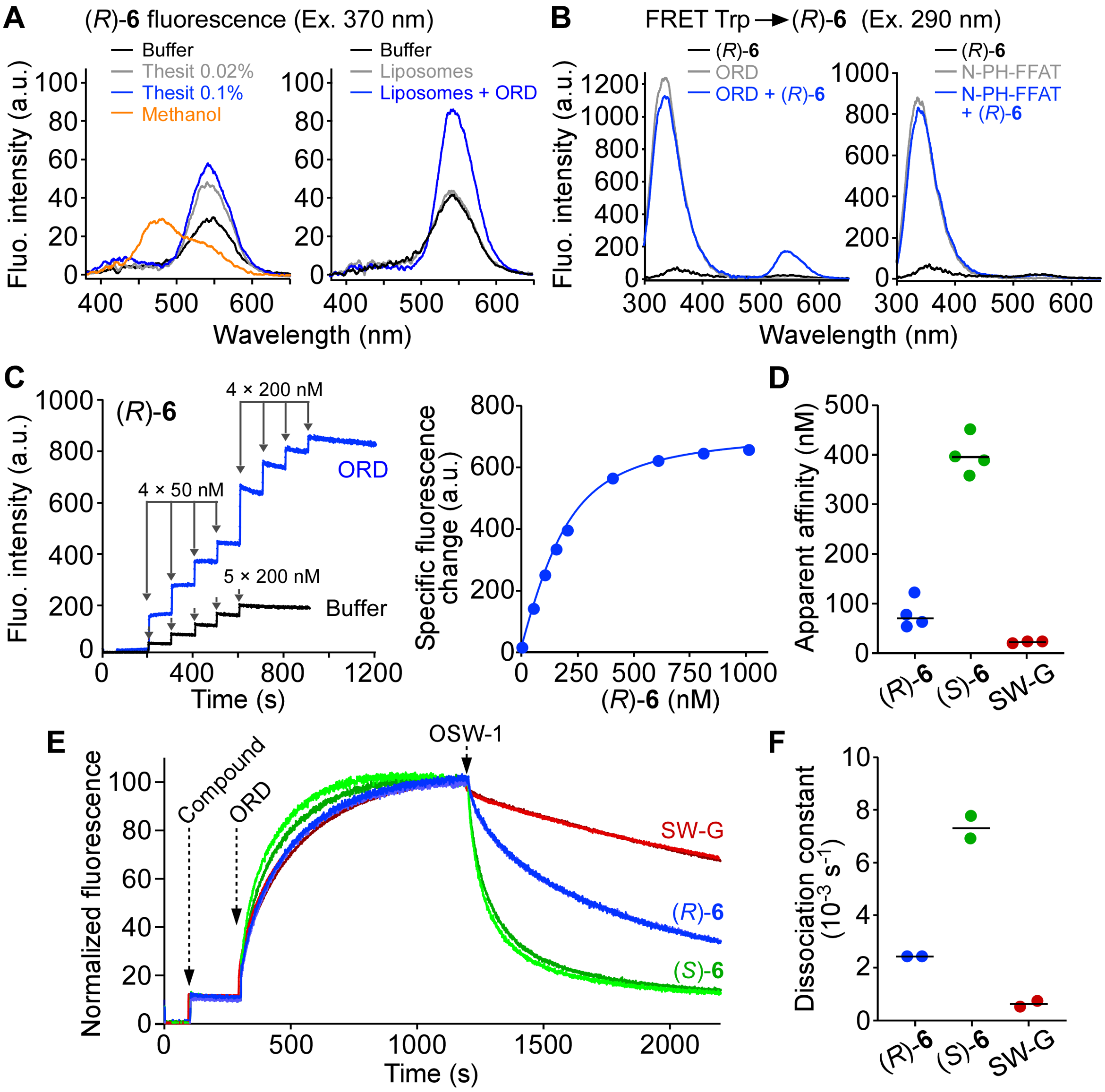

Figure 4. Fluorescence properties of (*R*)-**6** and (*S*)-**6** enable affinity and dissociation rate constant determination. **A.** Emission spectra of (*R*)-**6** (200 nM) upon excitation at 370 nm in methanol or in the presence of the indicated amount of Thesit® in HKM buffer (left panel), or in the presence of PC liposomes (100 µM), with or without ORD (200 nM) in HKM buffer (right panel). **B.** Emission spectra of (*R*)-**6** (200 nM) upon FRET excitation at 290 nm in the presence of PC liposomes (100 µM) with or without ORD (200 nM) (left panel) or N-PH-FFAT (200 nM) (right panel) in HKM buffer. **C.** Example of binding measurement of (*R*)-**6** to ORD under FRET conditions (left panel). Increasing amount of (*R*)-**6** was added in HKM buffer containing Thesit® (0.02%) in presence (blue curve) or absence (black curve) of ORD (200 nM). The right panel shows the corrected fluorescence increase of (*R*)-**6** bound to ORD after deduction of (*R*)-**6** fluorescence increase without ORD at the same concentration. **D.** Curve fit allows determination of (*R*)-**6** apparent affinity for ORD. Affinity measurements of (*S*)-**6** and SW-G for ORD under the same conditions are detailed in Fig S1. **E.** Time course of (*R*)-**6**, (*S*)-**6** and SW-G (200 nM) (blue, green and red curves, respectively) binding to the ORD (200 nM), and release upon OSW-1 addition (500 nM) as measured by FRET (excitation 290 nm; emission 550 nm for (*R*)-**6** and (*S*)-**6**; excitation 280 nm; emission 410 nm for SW-G). The reaction was performed in the presence of PC liposomes (100 µM). Maximum fluorescence intensity was normalized to 100 for comparison between the three compounds. **F.** Dissociation constants after OSW-1 addition were determined by mono exponential fitting of the curves in **E**.

To confirm the specific binding of compounds **6** to ORD, we performed fluorescence resonance energy transfer (FRET) experiments. We previously demonstrated that tryptophan (Trp) residues located in the vicinity of the lipid binding cavity of the ORD were close enough to SW-G to form fluorophore pairs, which resulted in a FRET signal [23]. We thus compared the emission spectra of the ORD alone, of compounds (*R*)- or (*S*)-**6** alone, and of mixtures containing stoichiometric amounts of both ORD and (*R*)- or (*S*)-**6** upon Trp excitation at 290 nm. As shown in Fig. 4B and S1E (left panels), the emission signal at 550 nm of (*R*)- or (*S*)-**6** had a ~10-fold higher intensity in the presence of ORD (colored curves) as compared to (*R*)- or (*S*)-**6** alone. As a control, we performed the same experiments with the membrane tethering region of OSBP (N-PH-FFAT; res. 1-408) instead of the ORD (Fig. 4B, S1E, right panels). Under these conditions, no FRET was observed. These experiments demonstrated that both (*R*)- and (*S*)-**6** molecules bind specifically to the ORD of OSBP.

We next used this specific FRET signal to assess the affinity of both enantiomers of macarangin B **6** for the ORD. These experiments were performed in the presence of Thesit® micelles, which allow very fast ligand exchange kinetics within the ORD [23], thus facilitating rapid equilibration. The increase in signal, upon the addition of an incremental amount of each compound, was measured both in the absence and presence of the ORD (Fig. 4C, left panel and Fig. S1F). The specific FRET signals obtained for (*R*)- and (*S*)-**6** were then plotted against compound concentration (Fig. 4C, right panel and Fig. S1G), and curve fitting enabled determination of their apparent affinity for ORD (Fig. 4D and Table 1). For comparison, a similar experiment was performed with SW-G **5** but at a different emission wavelength (Fig. S1C,F,G). The affinity of (*R*)-**6** (80 ± 30 nM) for ORD was five times higher than that of (*S*)-**6** (401± 38 nM), but four times lower than SW-G (22 ± 2 nM) (Fig. 4D).

We then performed FRET experiments to monitor the time course of (*R*)-**6**, (*S*)-**6** and SW-G binding into the ORD, as well as their dissociation constants upon competition with an excess of OSW-1, which is not fluorescent (Fig. 4E). These experiments were performed in the presence of PC liposomes, which, in contrast to Thesit® micelles, resulted in slow ligand exchange kinetics that could be readily resolved. The association kinetics of (*R*)-**6,** (*S*)-**6** and SW-G were similar, probably because of the rate-limiting dissociation of the initially bound cholesterol. By contrast, dissociation kinetics of (*R*)-**6,** (*S*)-**6** and SW-G upon OSW-1 addition showed significant differences. Dissociation of (*R*)-**6** (k_{off} = 24.10^{-4} s^{-1}) was three times slower than that of (*S*)-**6** (73.10^{-4} s^{-1}) but four times faster than that of SW-G **5** (6.10^{-4}s^{-1}). These relative differences in k_{off} are parallel to those observed for the apparent K_d of the compounds in the presence of Thesit®. Altogether, these experiments demonstrate that macarangin B **6** exhibits enantioselective binding to OSBP. As a result, (*R*)-**6**, (*S*)-**6** and SW-G form a series of ORD inhibitors with distinct affinities that extend over a 25-fold range.

Direct imaging of macarangin B (*R*)-6 and (*S*)-6 shows their specific interaction with OSBP in cells

We next took advantage of the fluorescence properties of (*R*)-**6** and (*S*)-**6** to directly visualize them in a cellular context using a confocal microscope (Fig. 5A, S2). hTERT-RPE-1 cells (hereafter RPE-1) were transiently transfected with OSBP-mCherry and then treated with (*R*)-**6** or (*S*)-**6** (2 µM) for 30 min at 37 °C. Strikingly, both compounds co-localized well with OSBP-mCherry and the TGN marker TGN-46 (Fig. 5B). (*R*)-**6** and (*S*)-**6** also labeled other intracellular regions, albeit weakly, most likely due to their partial hydrophobicity. Interestingly, their fluorescence level at the TGN perfectly correlated with that of OSBP-mCherry (Fig. 5C), suggesting that cellular incorporation of (*R*)-**6** and (*S*)-**6** largely depends on OSBP. Moreover, co-treatment with the non-fluorescent compound OSW-1 **4** prevented TGN labeling by (*R*)- or (*S*)-**6** (Fig. 5B, C, bottom panels). We also noticed that compound (*S*)-**6** accumulated slightly less at the TGN than (*R*)-**6**, in good agreement with their respective affinity for OSBP measured *in vitro* (Fig. 4C).

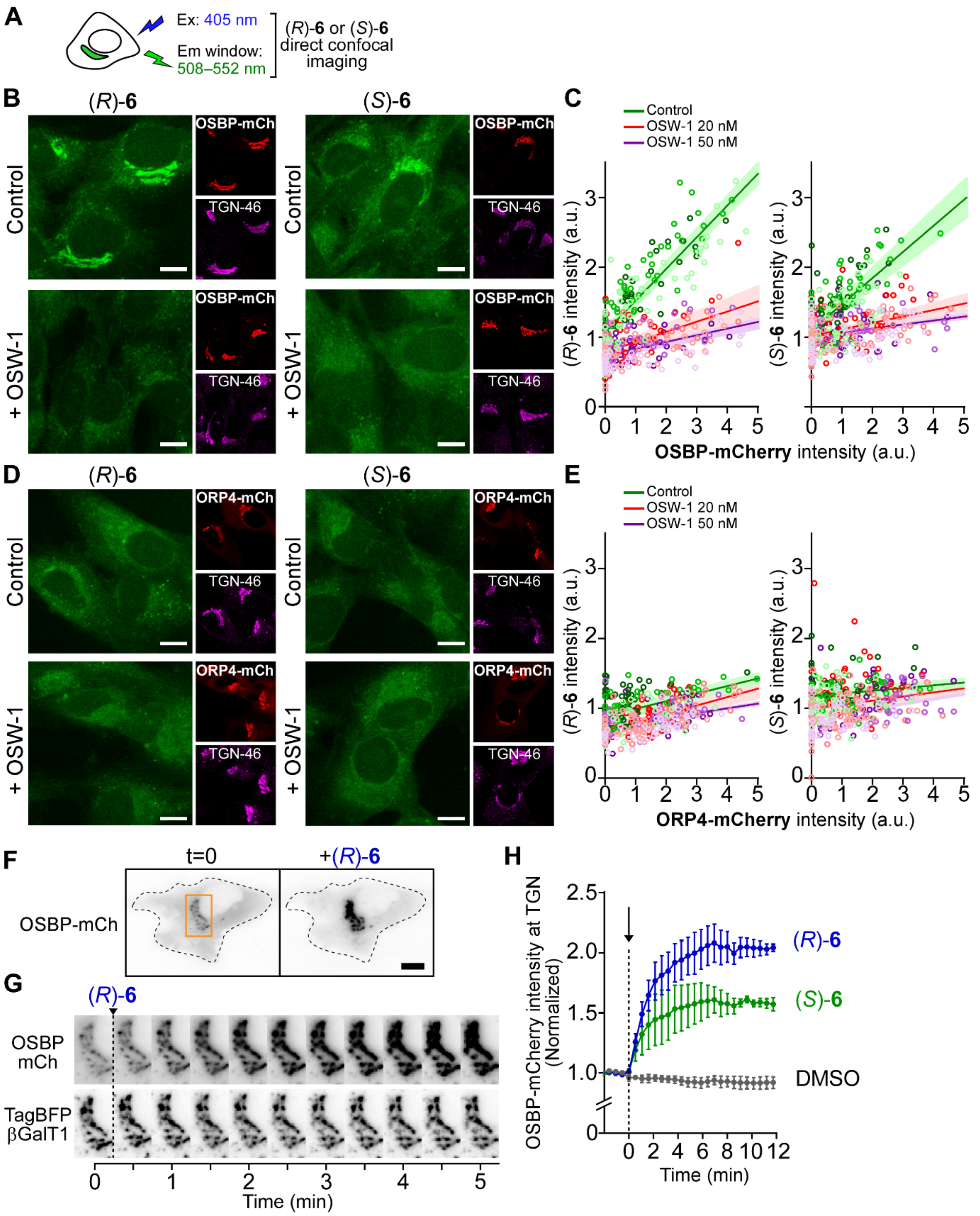

Figure 5. Direct fluorescent imaging of macarangin B (*R*)-**6** and (*S*)-**6** and their effect on OSBP dynamics. **A.** Sketch summarizing the microscope settings used to observe the compounds. **B.** Confocal images of RPE-1 transfected with OSBP-mCherry for 18 h, labelled with either (*R*)-**6** or (*S*)-**6** (2 μM) for 30 min in the presence of DMSO (control) or OSW-1 (20 nM), then fixed, permeabilized and immunolabelled with anti-TGN-46. Scale bars: 10 μm**. C.** (*R*)-**6** (left panel) or (*S*)-**6** (right panel) fluorescence intensity at the TGN as a function of OSBP-mCherry expression levels in the presence of the indicated amount of OSW-1. Measurements were performed on 130–160 cells for each condition. Curves and shaded area are mean ± SE of linear fits from 3 independent experiments. **D**, **E.** Same experiments as presented in **B** and **C** except that RPE-1 cells were transfected with ORP4-mCherry. Measurements were performed on 125–145 cells for each condition. Curves and shaded area are mean ± SE of linear fits from 3 independent experiments. Scale

bars: 10 µm. **F.** Time-lapse microscopy of RPE-1 cells co-transfected with OSBP-mCherry and the TGN marker TagBFP-βGalT1 for 18 h and treated with (*R*)-**6** (500 nM). **G.** Individual frames from a time series featuring the TGN area of the cell showed in **F.** Upon (*R*)-**6** addition, OSBP rapidly concentrates to βGalT1-positive perinuclear regions. Scale bar: 10 µm. **H.** Normalized intensity of OSBP-mCherry at the TGN. The arrow indicates the addition of compounds (*R*)-**6** (blue curve), (*S*)-**6** (green curve) or DMSO as control (grey curve) to the extracellular medium. Curves are mean ± SE of 3 independent experiments with 14 to 18 kinetics each.

Since most ORPphilins, but not SWs, bind not only to OSBP but also to its closest ortholog ORP4 [17], we also transfected RPE-1 cells with ORP4-mCherry. We further measured the cellular incorporation of macarangin B **6** enantiomers in order to assess their target specificity. Our results indicated that ORP4 overexpression did not help recruit (*R*)-**6** or (*S*)-**6** to TGN (Fig. 5D, E), thus demonstrating that these compounds prefer to interact with OSBP.

As previously described, OSBP is strongly recruited to ER/TGN MCS upon inhibition by ORPphilins. This effect is due to the accumulation of PI(4)P produced by PI-4-kinases in TGN membranes, which is no longer transported to the ER by OSBP and hydrolyzed by the phosphatase Sac1 [22]. The difference between compounds (*R*)-**6** and (*S*)-**6** in their affinity for OSBP (Fig. 4C) prompted us to compare their ability to recruit OSBP-mCherry to the perinuclear region, where ER/TGN MCSs were observed by live cell imaging. In control RPE-1 cells, OSBP-mCherry was mostly cytosolic and decorated slightly the TGN marked by TagBFP-βGalT1 (Fig. 5F, left panel). Upon (*R*)-**6** addition to the extracellular medium, OSBP-mCherry rapidly relocated to the TGN at the expense of the cytosolic pool ($t_{1/2}$ = 1.28 min), suggesting that (*R*)-**6** rapidly crosses cell membranes to inhibit PI(4)P transport and hydrolysis (Fig. 5G, H). This was confirmed by direct imaging of (*R*)-**6** alongside OSBP at the TGN just 1 min after its addition to the extracellular medium (Fig. S2). Interestingly, (*S*)-**6** addition also caused a rapid shift ($t_{1/2}$ = 1.11 min) of the OSBP pool towards the TGN, except that in this case, the increase in TGN-associated OSBP-mCherry fluorescence was significantly lower (1.6- and 2.1-fold increase, respectively with (*S*)-**6** and (*R*)-**6**) (Fig. 5H). Taken together, these experiments demonstrate that both macarangin B **6** enantiomers act directly on OSBP at the TGN. However, compound (*R*)-**6**, which has a better affinity for OSBP, concentrates in the perinuclear region and impacts OSBP dynamics and activity more strongly than (*S*)-**6**.

Molecular dynamics simulations suggest that macarangin B (*R*)-6 and (*S*)-6 adopt different orientations in OSBP

Considering the different biochemical and cellular properties of the two macarangin B **6** enantiomers, we further investigated their interaction with OSBP at the structural level using computational approaches. We first performed docking simulations of cholesterol (as a control), (*R*)-**6**, (*S*)-**6**, SW-G and OSW-1 to the known crystal structure of the OSBP ORD (PDB: 7V62 [31]) (see Methods). Docking was run with AutoDock, which ranks clusters of target-ligand poses using energy-based scoring. Analysis showed that cholesterol, SW-G, OSW-1 and (*S*)-**6**, but not (*R*)-**6**, bind to ORD according to single conformations. In agreement with the OSBP:cholesterol crystal structure, the hydroxyl group of cholesterol was oriented towards the bottom of the ORD cavity [31], as was that of the SW-G HHX moiety, consistent with previous SAR studies [35]. We found that the HHX of (*S*)-**6** was similarly oriented.

Unexpectedly, two large clusters of low-energy poses were obtained for compound (*R*)-**6**, showing two possible orientations ("up" and "down") within the ORD pocket. The best pose conformations for each ligand (*i.e.*, with the most favorable binding energy values) were then used to perform all-atom molecular dynamics (MD) simulations (Fig. 6A, S3A). All compounds remained in the OSBP ORD binding pocket throughout the simulations. Estimation of the interaction energies indicated similar stability of cholesterol, (*R*)-**6** and (*S*)-**6** in the ORD pocket (Fig. 6B). Notably, no significant difference was found between values for (*R*)-**6** "up" and "down" orientations, suggesting that there is no conformational preference for this interaction. These data also confirmed that SW-G and especially OSW-1 form highly stable complexes with OSBP ORD. To assess whether the compounds influence the stability of the ORD, we next calculated the root-mean-square fluctuation (RMSF) of the residues involved in the ligand binding region over the simulation time in the presence of the different compounds (Fig. S3B,C). To facilitate the analysis, RMSF results were normalized to values obtained with cholesterol. The results showed that different sub-regions became more flexible (higher RMSF values) or conversely more stable (when RMSF values decreased) depending on the bound compound. In particular, residues from the lid (aa. 415-451) showed greater flexibility with (*R*)-**6** “down” and SW-G, but not with (*R*)-**6** “up” and (*S*)-**6**, compared to cholesterol (Fig. S3C). By contrast, OSW-1 strongly stabilized all residues of the ligand binding region. To better understand these differences, we analyzed the formation of hydrogen bonds (H-bonds) between each molecule and the ORD as well as their occupancy during simulations (Fig. 6C). H-bonds frequently occurred between Lys577 and cholesterol (38.8 % of the simulation time), (*R*)-**6** “down” (14.9 %) and (*S*)-**6** (20.8 %), whereas (*R*)-**6** “up” was involved in an OH–π H-bonding with the aromatic ring of Phe440 (18.4 %) (Fig. 6A,C, Movies S1–3). In comparison, SW-G and OSW-1 formed two, three or even more H-bonds with ORD residues, with much higher frequency (up to 56.2 % of the time between OSW-1 and Ser547), thereby explaining their stronger interaction with the ORD (Fig. 6C, S3A).

To experimentally test the contribution of the H-bonding residues Lys577 and Phe440 in the interaction between OSBP and macarangin B **6** enantiomers, we transfected RPE-1 cells with OSBP-mCherry constructs containing or not the point mutations K577A or F440A, and analyzed with a confocal microscope the fluorescence distribution of (*R*)- or (*S*)-**6** upon cell treatment (Fig. 6D). As observed before, (*R*)- and (*S*)-**6** concentrated with OSBP-mCherry WT in the TGN region, and the compounds’ fluorescence level correlated with that of OSBP-mCherry (Fig. 6E), indicating that (*R*)- and (*S*)-**6** bind to OSBP (see also Fig. 5B,C). By contrast, the K577A and F440A mutations strongly reduced the ability of (*R*)- and (*S*)-**6** to co-distribute with OSBP, indicating that these residues play a significant role in these interactions. Although our *in silico* analysis predicted that F440 formed a H-bond only with (*R*)-**6**, the F440A mutation also interfered with (*S*)-**6** and SW-G binding to a significant extent (Fig. 6D,E, S4), suggesting that F440 promotes hydrophobic interactions with these ligands.

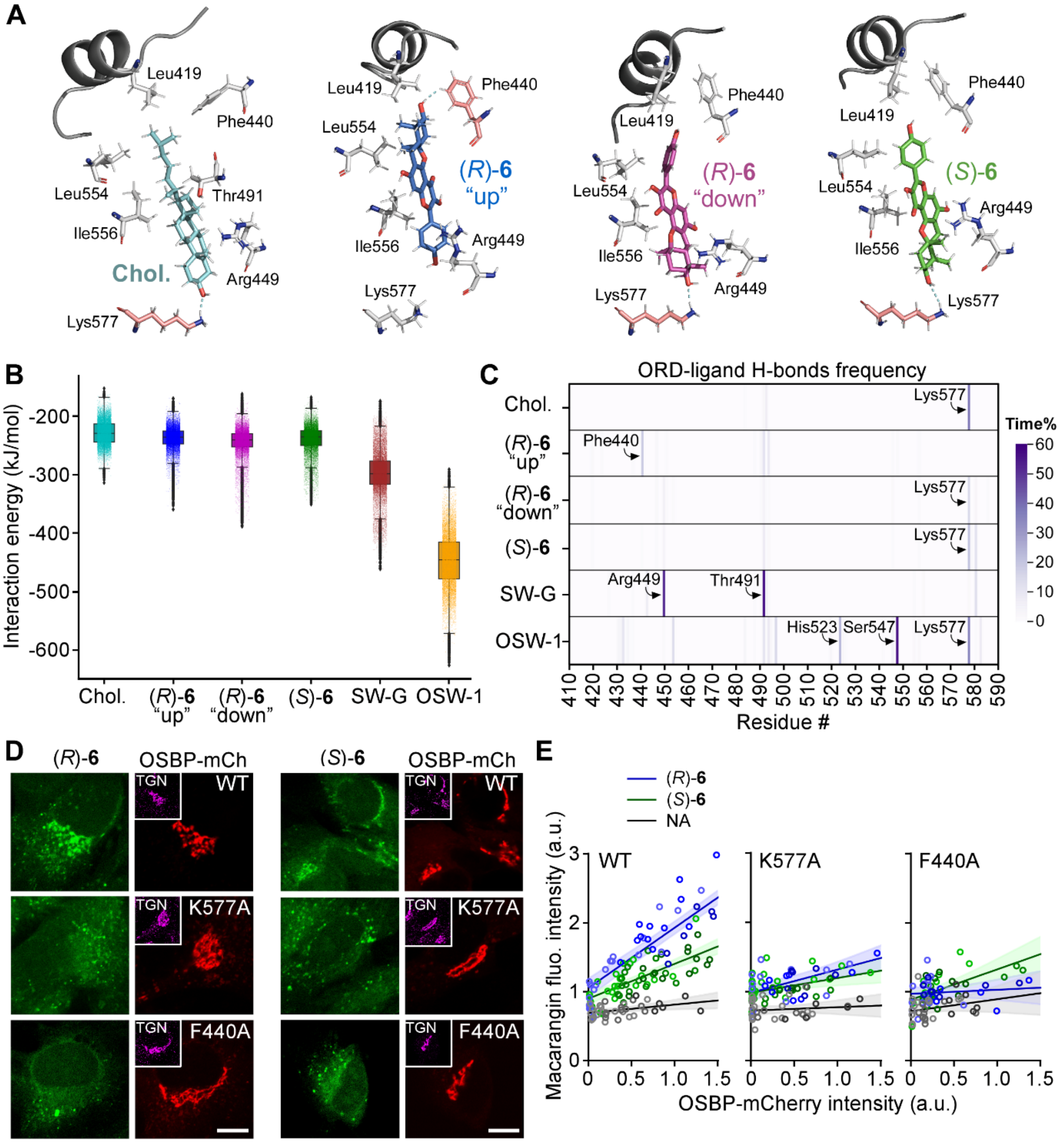

Figure 6. MD simulations of ORPphilins in OSBP ORD domain. **A-C.** Results are averaged over three replicates of 500-ns simulation for each complex. **A.** Most representative conformations of cholesterol, (*R*)-**6** "up", (*R*)-**6** "down" and (*S*)-**6** in the ORD pocket, as obtained from clustering the simulations of each compound. Residues that frequently form H-bonds with ligands are colored in pink. **B.** Interaction energy between ligands and the ORD. One point represents one simulation frame. **C.** H-bond frequency between the indicated ligands and ORD pocket residues expressed in percentage of simulation time. **D.** Confocal images of RPE-1 cells transfected with OSBP-mCherry WT, K577A or F440A, labelled with either (*R*)-**6** or (*S*)-**6** (2 µM) for 30 min, then fixed, permeabilized and immunolabelled with anti-TGN-46. Scale bar: 10 µm. **E.** Quantification of (*R*)-**6** (blue), (*S*)-**6** (green) and control (no labelling, grey) fluorescence intensity at the TGN as a function of the expression level of the indicated OSBP-mCherry constructs. Measurements were performed on 30–56 cells for each condition. Curves and shaded area show mean ± SE of linear fits from 3 independent experiments.

Taken together, our results indicate that macarangin B **6** enantiomers associate differentially with the ORD of OSBP at the structural level, (*R*)-**6** being able to take two different orientations, and that H-bonds play a crucial role in maintaining these compounds in the pocket. These findings further indicate that (*R*)- and (*S*)-macarangin B **6** are specific OSBP inhibitors and that they do not interact with OSBP as tightly as SW-G and OSW-1.

Macarangin B (*R*)-6 and (*S*)-6 have low cytotoxicity and potent antiviral properties

Next, we sought to evaluate the cytotoxicity of (*R*)- and (*S*)-**6**. As previously described, SWs show a distinctive cytotoxicity profile on the NCI-60 cancer cell line screen, with highly sensitive cell lines (*e.g.*, derived from the CNS like U87-MG) and low-responsive ones (such as A549 lung cells). Of note, the activity pattern of unnatural (*S*, *S*, *S*) enantiomers of SWs was shown to correlate poorly with that of natural (*R*, *R*, *R*)-series on the NCI-60 cell lines [45]. We used a panel of eight cell lines to assess (*R*)- and (*S*)-**6** cytotoxicity, which was also compared to that of SW-G and OSW-1 (Fig. 7A). Strikingly, (*R*)-**6** and (*S*)-**6** showed cytotoxicity in the micromolar range, significantly lower than that measured with SW-G and OSW-1. Surprisingly, however, the stereochemistry of the HHX moiety had little impact on cytotoxicity, as (*R*)-**6** and (*S*)-**6** showed roughly the same IC_{50} on all cell lines, contrasting with their distinct affinities for OSBP. Furthermore, we could highlight a strong decorrelation between OSBP affinity and cytotoxicity, particularly on U87-MG: (*R*)-**6** was 300 times less cytotoxic than SW-G while its affinity for OSBP is reduced only fourfold (Fig. 4D, 7A). This difference in cytotoxicity is unlikely to be due to cell penetration issues, as indicated by our live cell imaging experiments (Fig. S2) and suggests instead that SW-G-mediated cell death pathway might be, at least partially, OSBP-independent.

OSBP was previously shown to play an essential role in the growth of positive single-stranded RNA viruses, such as flaviviruses or enteroviruses, by promoting the biogenesis of organelle-like structures, which serve as platforms for the viral replication machinery [30]. Previous studies showed that OSW-1 potently inhibits the replication of various enteroviruses [57]; however, its high cytotoxicity likely hinders its application as an antiviral. Given that compounds (*R*)- and (*S*)-**6**, and, to a lesser extent, SW-G, are much less cytotoxic than OSW-1 but interact with a good affinity with OSBP, we wondered whether they could inhibit the growth of the flavivirus ZIKV in human epithelial A549 cells with similar efficacy but a much higher selectivity index.

We first determined the concentration range of the compounds (*R*)-**6**, (*S*)-**6**, SW-G and OSW-1 at which we could perform antiviral assays without inducing toxicity on host cells. For this, we treated A549 cells for 24, 48 and 72 h with increasing concentrations of each compound and evaluated cell metabolic activity by MTT assays (Fig. S5A). Compounds (*R*)- and (*S*)-**6**, as well as SW-G, were not cytotoxic after 24 h up to 20 µM concentration and compounds (*R*)- and (*S*)-**6** did not affect cell viability at 72 h post-addition up to 2 µM. By contrast, at 48 and 72 h post-addition, OSW-1 induced cytotoxicity at nanomolar concentrations, whereas SW-G affected cell viability at micromolar concentrations. Therefore, we chose a maximum dose of 2 µM for a 24-hour treatment with each of the inhibitors for the following experiments. To evaluate their antiviral activity against ZIKV, A549 cells were infected with the French Polynesia 2013 epidemic strain and incubated 24 h with increasing doses of each compound up to 2 µM. We observed that at 200 nM, SW-G, (*R*)- and (*S*)-**6** reduced extracellular viral progeny production by 2 decimal logs ($\log_{10}$), whereas OSW-1 showed much weaker antiviral activity (Fig. 7B). We next determined whether the anti-ZIKV effect was attributable to a decrease in viral RNA replication. As shown in Fig. 7C, all inhibitors induced a dramatic reduction in RNA production, as measured by RT-qPCR, suggesting that these compounds act at late stages of viral infection. Nevertheless, they showed notable differences in activity: 20 nM of SW-G, (*R*)-**6** and (*S*)-**6** were sufficient to reduce the amount of viral RNA in ZIKV-infected A549 cells by at least 2 $\log_{10}$s, whereas a 100-fold higher concentration of OSW-1 (2 µM) was required to achieve similar inhibition. Furthermore, (*R*)-**6** and SW-G were more effective in suppressing viral RNA production in ZIKV-infected cells than (*S*)-**6**.

To determine whether the higher activity of (*R*)-**6** and SW-G was related to their higher affinity for OSBP, A549 cells were transfected either with OSBP-mCherry or ORP4-mCherry before infection with ZIKV (Fig. 7D, S5B). Previous studies have shown that cell sensitivity to ORPphilins strongly correlated with OSBP expression level: cell lines with high amounts of endogenous OSBP, or overexpressing OSBP, were more resistant to ORPphilin treatment, suggesting a titration effect [17,23]. In agreement with this, we found that overexpressing OSBP-mCherry attenuated the antiviral activity of (*R*)-**6**, (*S*)-**6**, SW-G and OSW-1 (Fig. 7E). In this case, all four compounds decreased the viral titer similarly by ~1.5 $\log_{10}$s compared with untreated cells, whereas a decrease of up to 2.5 $\log_{10}$s was obtained without OSBP overexpression (Fig. 7B). We then performed the same analyses with ZIKV-infected A549 cells transfected with ORP4-mCherry (Fig. 7F). Surprisingly, upon ORP4-mCherry overexpression viral growth increased by one $\log_{10}$ as compared to non-transfected cells or cells transfected with an EGFP-expressing plasmid. Nevertheless, virus progeny production was strongly reduced by up to 2.4 $\log_{10}$s in the presence of (*R*)-**6** and SW-G, and by 2 $\log_{10}$s with (*S*)-**6**. Of note, this reduction was less pronounced with OSW-1, reflecting its weaker antiviral effect, as seen in Fig. 7B, and probably because both OSBP and ORP4 titrate OSW-1, resulting in less inhibition when ORP4 is overexpressed.

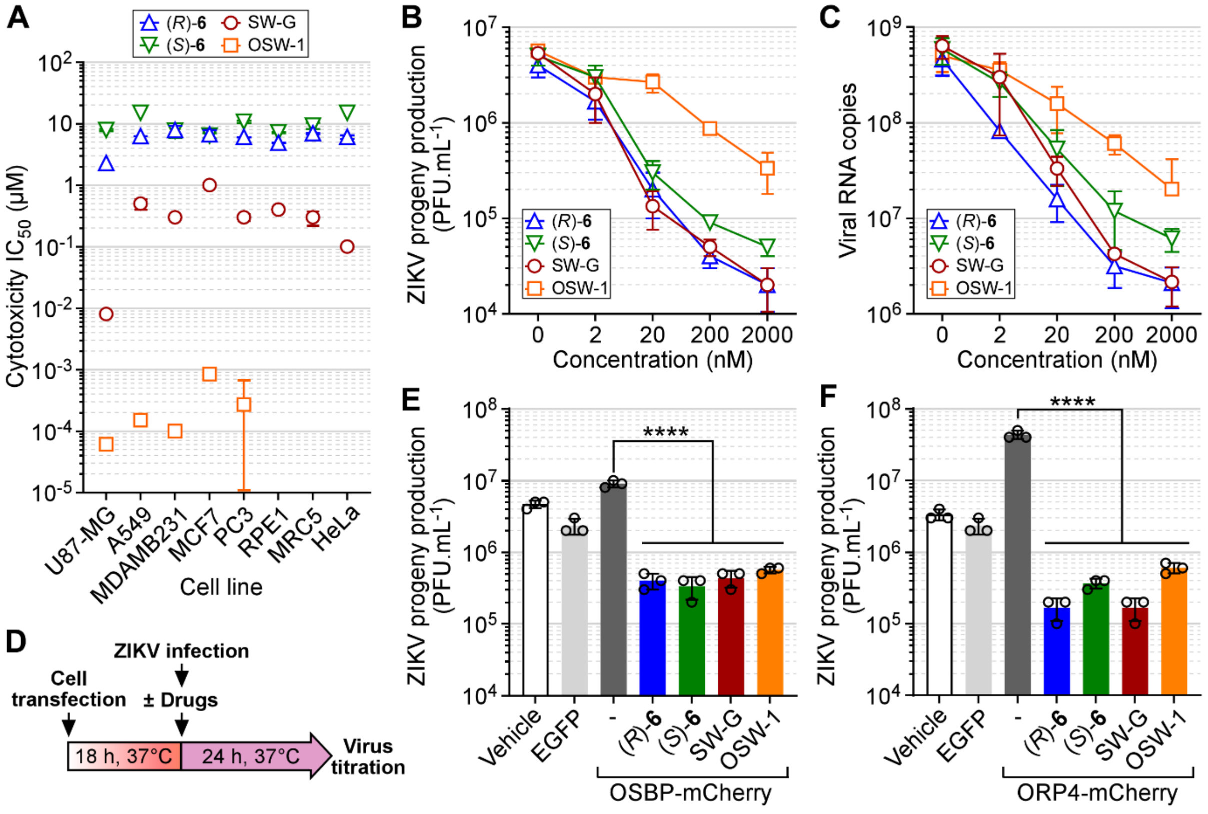

Figure 7. (R)-**6** and (S)-**6** are weakly cytotoxic and prevent cellular infection by epidemic strain of ZIKV. **A.** Cytotoxicity on a panel of eight cell lines of (R)-**6** and (S)-**6** compared to SW-G and OSW-1. Data represent means ± SD from three independent experiments. **B-C.** A549 cells were infected with ZIKV (PF-25013-18) at MOI of 2 and continuously incubated with increasing concentrations (0–2000 nM) of (R)-**6**, (S)-**6**, SW-G or OSW-1. **B.** ZIKV progeny production was quantified by plaque-forming assay. **C.** The amount of viral genomic RNA in ZIKV-infected cells was determined by RT-qPCR. Data represent means ± SD from four

independent experiments. **D.** Protocol for synchronized cell transfection followed by ZIKV infection and drug treatment. **E.** A549 cells were transfected with EGFP alone (light grey) or OSBP-mCherry. 18 h post-transfection, drugs (20 µM, colored bars) or DMSO (dark grey) were used for treatment throughout the infection. 24 h post-infection, the virus titer was evaluated by plaque forming assay. Data represent the means ± SD from three independent experiments. One-way ANOVA and Dunnett's test (*** p<0.001). **F.** Same as **E** with ORP4-mCherry instead of OSBP-mCherry.

Taken together, these results demonstrate that (*R*)-**6**, which has a higher affinity than (*S*)-**6** for OSBP but lower than SW-G and OSW-1, couples its specificity towards OSBP to strong anti-ZIKV activity. Given its straightforward synthesis and its low cytotoxicity, we consider macarangin B (*R*)-**6** to be a promising antiviral agent.

Discussion

In this study, we isolated from a Vietnamese bushy tree a new racemic compound, macarangin B **6**, bearing a rare hydroxy-HHX moiety, which has been described only for the SW derivatives so far. SWs, like other families of natural compounds, have been named ORPphilins because they bind to and inhibit OSBP. We have shown that macarangin B **6** inhibits the sterol-transfer activity of OSBP *in vitro* as effectively as other ORPphilins (Fig. 2). Since it was isolated at a very small scale, and considering that the absolute configuration of the HHX motif of SWs influences their biological properties [46], we performed the asymmetric synthesis of the two enantiomers (*R*, *R*, *R*) and (*S*, *S*, *S*) of macarangin B **6**. A bio-inspired strategy provided a concise and cost-effective approach to obtain compounds (*R*)-**6** and (*S*)-**6** in only seven steps from natural kaempferol **9** (Fig. 3), which contrasts with the complex syntheses required for other ORPphilins [32-35]. In particular, the hydroxy-HHX moiety was efficiently elaborated by an enantioselective polyene cyclisation of (*R*)-**13** or (*S*)-**13** chiral epoxides. Using the fluorescent properties conferred by their 3-hydroxy-flavone scaffold, we performed equilibrium and kinetic measurements by FRET between OSBP ORD tryptophans and (*R*) and (*S*) enantiomers of macarangin B **6**. We showed that both bind the ORD domain of OSBP, albeit with distinct affinities: in the tens of nanomolar range for (*R*)-**6** and in the sub-micromolar range for (*S*)-**6** (Fig. 4C-F). Consistently, (*R*)-**6** can be regarded as an eutomer and (*S*)-**6** as a distomer [58]. Compared with SW-G, (*R*)-**6** and (*S*)-**6** displayed a 4-fold and 15-fold reduced affinity for the ORD and could be displaced by OSW1, another ORPphilin. Since this latter has a stronger affinity than SW-G, the four compounds form a repertoire of OSBP inhibitors with a wide range of affinities and residence times in the ORD, which may facilitate future cellular and physiological studies and applications.

The emission of (*R*)-**6** and (*S*)-**6** in the visible spectrum enabled us to precisely define their intracellular distribution close to OSBP in the TGN region. Moreover, their accumulation in cells varied as a function of OSBP expression levels but not ORP4, indicating that (*R*)-**6** and (*S*)-**6** are selective towards OSBP (Fig. 5A-E). In addition, (*R*)-**6** had a stronger tendency to concentrate at the TGN and showed a more potent effect in recruiting OSBP at ER/TGN MCS compared to (*S*)-**6**. *In silico* approaches further indicated that the binding site for (*R*)-**6** and (*S*)-**6** overlapped with the sterol-binding site into the hydrophobic cavity of the ORD. Most interestingly, molecular docking and MD simulations predicted that (*R*)-**6**, but not (*S*)-**6**, is able to adopt two different orientations within the ORD binding site (Fig. 6A). Depending on its orientation, (*R*)-**6** was allowed to form H-bonds either with F440, which is close to the entrance of the pocket, or with K577, located at the very bottom of the pocket. K577 also formed an H-bond with (*S*)-**6** very frequently during simulations. Site-directed mutagenesis confirmed the importance of these two residues in the interaction with macarangin B **6** enantiomers.

Taken together, the structural, biochemical and cellular properties of macarangin B **6** described here classify this molecule as a new member of the ORPphilin family (Fig. 1). However, all ORPphilins described so far show a similar pattern of sensitivity against the NCI 60 cancer cell lines and are highly cytotoxic for specific cell lines, such as glioblastoma [5-16]. By contrast, compounds (*R*)-**6** and (*S*)-**6** had a lower cytotoxicity (Fig. 7A), which did not correlate with their affinity for OSBP. These results sharply deviate from our recent findings on various SW derivatives, where a good parallel between Ki for OSBP and cytotoxicity on MG U-87 cells was observed, with the highest affinity for OSBP coinciding with maximum cytotoxicity [59]. Moreover, whereas the absolute configuration of the HHX moiety of (*R*)- and (*S*)-**6** influenced their affinity for OSBP, it had no impact on their cytotoxicity, which was both modest and similar. This result also differs from the data obtained for SW-F, where the (*S*)-enantiomer was less cytotoxic than the (*R*)-enantiomer [45]. One plausible explanation is that, in addition to OSBP, the ORPphilins that have been previously described target other protein(s) that play a critical role in cell death. This hypothesis is reinforced by recent findings showing that OSBP deficiency had little effect on OSW-1-induced cell death in Neuro2a cells [60]. In fact, among ORPs, only ORP3, 4, 5 and 8 but not OSBP have been implicated in cell proliferation and tumor transformation [24]. For example, ORP4 is involved in hematologic malignancies [61]. Importantly, our overexpression experiments suggest that neither (*R*)-**6** nor (*S*)-**6** could bind to ORP4, indicating a high specificity of these compounds for OSBP. As ORP4 is the target of OSW-1 but not of SWs [23], these differences suggest that beyond OSBP, other target(s) responsible for their cytotoxicity remain to be identified.

Many RNA viruses, like flaviviruses, coopt the host lipid metabolic network to facilitate their replication. Notably, OSBP activity is hijacked by viruses to transport cholesterol in their replication organelles [26–31]. Evidence suggests that targeting OSBP by inhibitors blocks viral infection [26-31, 62] and this could be an attractive therapeutic approach to treat viral illnesses, like Zika fever. Indeed, ZIKV infection has become a pervasive viral disease, exerting a profound socio-economic influence yet lacking both vaccines and curative treatments [63]. Despite their good affinity for OSBP, ORPphilins are too cytotoxic to be used as antivirals. Various other non-natural OSBP inhibitors have been reported to have antiviral properties: TTP [64], AN-12-H5 [65], THEV [29] and itraconazole (ITZ) [28, 66]. Most of them were identified by chemical screening thanks to their anti-enterovirus activities. However, none is selective towards OSBP. The antiviral effect of AN-12-H5 is mediated by its interaction with OSBP but also with another unknown target [64]. The other compounds bind not only OSBP but also ORP4: THEV within the ORD [67] and ITZ and TTP through other unidentified binding sites [68]. As ORP4 plays a role in cancer cell survival and proliferation, an OSBP-selective molecule such as (*R*)-**6** is highly desirable for designing effective antiviral compounds. We showed that this compound had high anti-ZIKV activity (Fig. 7B, C) and, owing to its low toxicity, a high selectivity index. (*R*)-**6** also offers the advantage of being easy to modulate, making it a perfect hit for subsequent modifications. Our strategy is in line with the growing view that specifically targeting lipid metabolism pathways, in particular cholesterol metabolism, to interfere with flavivirus infection should provide effective antiviral therapeutic avenues [69].

Acknowledgement

We thank A. Patel and S. Abélanet (IPMC, Valbonne) for invaluable technical assistance; D. Lévy (Institut Curie, Paris), F. Alpy (IGBMC, Illkirch) and C. Etchebest (Université Paris Cité) and P. Despres (Université de la Réunion) for discussions, and all members of the Roussi and Antonny labs for their insights. We thank the IPMC Imaging and Cytometry facility, part of the MICA platform (GIS IBiSA). This work was supported by the CNRS, the Inserm, the Agence Nationale de la Recherche (ANR-21-CE13-0021-01), the ERC (Synergy #856404), two "Investissement d'Avenir" grants managed by Agence Nationale de la Recherche (UPSaclay ref. CDE-2019-002288 / IRE 2019-083 and CEBA, ANR-10-LABX-25-01), the "Investments for the Future" program LABEX SIGNALIFE (ANR-11-LABX-0028-01), and a maturation program grant managed by the SATT Paris-Saclay (CM2017-0045). G. J. and C. G. were supported by a PhD fellowship from the Université Paris Saclay (ED ITFA). Z.G. was supported by the Polytech Nice Sophia (Université Côte d'Azur) PhD fellowship program. J.H. received funding from PHYTODENGUE program (Région Réunion N° SYNERGIE: RE0028005).

References

1. Lautié E, Russo O, Ducrot P, *et al.* Unraveling Plant Natural Chemical Diversity for Drug Discovery Purposes. *Front. Pharmacol.* 2020 ; 11 : 397.

2. Rodrigues T, Reker D, Schneider P, *et al.* Counting on natural products for drug design. *Nat. Chem.* 2016 ; 8 : 531–541.

3. Lachance H, Wetzel S, Kumar K, *et al.* Charting, Navigating, and Populating Natural Product Chemical Space for Drug Discovery. *J. Med. Chem.* 2012 ; 55 : 5989–6001.

4. Rosén J, Gottfries J, Muresan S, *et al.* Novel chemical space exploration via natural products. *J. Med. Chem.* 2009 ; 52 : 1953–62.

5. Pettit GR, Inoue M, Kamano Y, *et al.* Antineoplastic agents. 147. Isolation and structure of the powerful cell growth inhibitor cephalostatin 1. *J. Am. Chem. Soc.* 1988 ; 110 : 2006–2007.

6. Fukuzawa S, Matsunaga S, Fusetani N. Isolation and structure elucidation of ritterazines B and C, highly cytotoxic dimeric steroidal alkaloids, from the tunicate Ritterella tokioka. *J. Org. Chem.* 1995 ; 60 : 608–614.

7. McCormick JL, McKee TC, Cardellina JH, *et al.* Cytotoxic Triterpenes from a Marine Sponge, Stelletta sp. *J. Nat. Prod.* 1996 ; 59 : 1047–1050.

8. Kubo S, Mimaki Y, Terao M, *et al.* Acylated cholestane glycosides from the bulbs of Ornithogalum saundersiae. *Phytochemistry* 1992 ; 31 : 3969–3973.

9. Thoison O, Hnawia E, Guiéritte-Voegelein F, *et al.* Vedelianin, a hexahydroxanthene derivative isolated from Macaranga vedeliana. *Phytochemistry* 1992 ; 31 : 1439–1442.

10. Beutler JA, Shoemaker RH, Johnson T, *et al.* Cytotoxic Geranyl Stilbenes from Macaranga schweinfurthii. *J Nat Prod* 1998 ; 61 : 1509–1512.

11. Beutler JA, Jato J, Cragg GM, *et al.* Schweinfurthin D, A Cytotoxic Stilbene from Macaranga schweinfurthii. *Nat Prod Lett* 2000 ; 14 : 399–404.

12. Klausmeyer P, Van QN, Jato J, *et al.* Schweinfurthins I and J from Macaranga schweinfurthii ⊥. *J Nat Prod* 2010 ; 73 : 479–481.

13. Kaaden JE van D, Hemscheidt TK, Mooberry SL. Mappain, a new cytotoxic prenylated stilbene from Macaranga mappa. *J. Nat. Prod.* 2001 ; 64 : 103–5.

14. Yoder BJ, Cao S, Norris A, *et al.* Antiproliferative Prenylated Stilbenes and Flavonoids from Macaranga alnifolia from the Madagascar Rainforest # ,1. *J Nat Prod* 2007 ; 70 : 342–346.

15. Péresse T, Jézéquel G, Allard P-M, *et al.* Cytotoxic Prenylated Stilbenes Isolated from Macaranga tanarius. *J Nat Prod* 2017 ; 80 : 2684–2691.

16. Rabow AA, Shoemaker RH, Sausville EA, *et al.* Mining the National Cancer Institute's Tumor-Screening Database: Identification of Compounds with Similar Cellular Activities. *J Med Chem* 2002 ; 45 : 818–840.

17. Burgett AWG, Poulsen TB, Wangkanont K, *et al.* Natural products reveal cancer cell dependence on oxysterol-binding proteins. *Nat Chem Biol* 2011 ; 7 : 639–647.

18. Wong LH, Gatta AT, Levine TP. Lipid transfer proteins: the lipid commute via shuttles, bridges and tubes. *Nat Rev Mol Cell Bio* 2019 ; 20 : 85–101.

19. Delfosse V, Bourguet W, Drin G. Structural and Functional Specialization of OSBP-Related Proteins. *Contact* 2020 ; 3 : 251525642094662.

20. Mesmin B, Bigay J, Moser von Filseck J, *et al.* A Four-Step Cycle Driven by PI(4)P Hydrolysis Directs Sterol/PI(4)P Exchange by the ER-Golgi Tether OSBP. *Cell* 2013 ; 155 : 830–843.

21. Subra M, Antonny B, Mesmin B. New insights into the OSBP–VAP cycle. *Curr Opin Cell Biol* 2023 ; 82 : 102172.

22. Mesmin B, Bigay J, Polidori J, *et al.* Sterol transfer, PI4P consumption, and control of membrane lipid order by endogenous OSBP. *Embo J* 2017 ; 36 : 3156–3174.

23. Péresse T, Kovacs D, Subra M, *et al.* Molecular and cellular dissection of the oxysterol-binding protein cycle through a fluorescent inhibitor. *J Biol Chem* 2020 ; 295 : 4277–4288.

24. Olkkonen VM. The emerging roles of OSBP-related proteins in cancer: Impacts through phosphoinositide metabolism and protein-protein interactions. *Biochem Pharmacol* 2022 ; 114455.

25. Zhong W, Lin W, Yang Y, *et al.* An acquired phosphatidylinositol 4-phosphate transport initiates T-cell deterioration and leukemogenesis. *Nat Commun* 2022 ; 13 : 4390.

26. Wang H, Perry JW, Lauring AS, *et al.* Oxysterol-Binding Protein Is a Phosphatidylinositol 4-Kinase Effector Required for HCV Replication Membrane Integrity and Cholesterol Trafficking. *Gastroenterology* 2014 ; 146 : 1373-1385.e11.

27. Meutiawati F, Bezemer B, Strating JRPM, *et al.* Posaconazole inhibits dengue virus replication by targeting oxysterol-binding protein. *Antivir Res* 2018 ; 157 : 68–79.

28. Strating JRPM, van der Linden L, Albulescu L, *et al.* Itraconazole Inhibits Enterovirus Replication by Targeting the Oxysterol-Binding Protein. *Cell Reports* 2015 ; 10 : 600–615.

29. Arita M, Kojima H, Nagano T, *et al.* Oxysterol-Binding Protein Family I Is the Target of Minor Enviroxime-Like Compounds. *J Virol* 2013 ; 87 : 4252–4260.

30. Strating JR, Kuppeveld FJ van. Viral rewiring of cellular lipid metabolism to create membranous replication compartments. *Curr Opin Cell Biol* 2017 ; 47 : 24–33.

31. Kobayashi J, Arita M, Sakai S, *et al.* Ligand Recognition by the Lipid Transfer Domain of Human OSBP Is Important for Enterovirus Replication. *Acs Infect Dis* 2022 ; 8 :1161-1170.

32. Boyko YD, Huck CJ, Sarlah D. Total Synthesis of Isomalabaricane Triterpenoids. *J. Am. Chem. Soc.* 2019 ; 141 : 14131–14135.

33. Nakayama Y, Maser MR, Okita T, *et al.* Total Synthesis of Ritterazine B. *J. Am. Chem. Soc.* 2021 ; 143 : 4187–4192.

34. Tang Y, Li N, Duan J, *et al.* Structure, Bioactivity, and Chemical Synthesis of OSW-1 and Other Steroidal Glycosides in the Genus Ornithogalum. *Chem Rev* 2013 ; 113 : 5480–5514.

35. Harmalkar DS, Mali JR, Sivaraman A, *et al.* Schweinfurthins A–Q: isolation, synthesis, and biochemical properties. *RSC Adv.* 2018 ; 8 : 21191–21209.

36. Allard P-M, Péresse T, Bisson J, *et al.* Integration of Molecular Networking and In-Silico MS/MS Fragmentation for Natural Products Dereplication. *Anal Chem* 2016 ; 88 : 3317–3323.

37. Alseekh S, Souza LP de, Benina M, *et al.* The style and substance of plant flavonoid decoration; towards defining both structure and function. *Phytochemistry* 2020 ; 174 : 112347.

38. Yang X, Jiang Y, Yang J, *et al.* Prenylated flavonoids, promising nutraceuticals with impressive biological activities. *Trends Food Sci. Technol.* 2015 ; 44 : 93–104.

39. Botta B, Vitali A, Menendez P, *et al.* Prenylated Flavonoids: Pharmacology and Biotechnology. *Curr. Med. Chem.* 2005 ; 12 : 713–739.

40. Huang Y-C, Hwang T-L, Chang C-S, *et al.* Anti-inflammatory Flavonoids from the Rhizomes of Helminthostachys zeylanica. *J. Nat. Prod.* 2009 ; 72 : 1273–1278.

41. Huang Y-L, Yeh P-Y, Shen C-C, *et al.* Antioxidant flavonoids from the rhizomes of Helminthostachys zeylanica. *Phytochemistry* 2003 ; 64 : 1277–1283.

42. Barrett A, Ma T-K, Mies T. Recent Developments in Polyene Cyclizations and Their Applications in Natural Product Synthesis. *Synthesis* 2018 ; 51 : 67–82.

43. Stork G, Burgstahler AW. The Stereochemistry of Polyene Cyclization. *J. Am. Chem. Soc.* 1955 ; 77 : 5068–5077.

44. Eschenmoser A, Ruzicka L, Jeger O, *et al.* Zur Kenntnis der Triterpene. 190. Mitteilung. Eine stereochemische Interpretation der biogenetischen Isoprenregel bei den Triterpenen. *Helvetica Chim. Acta* 1955 ; 38 : 1890–1904.

45. Hnawia E, Thoison O, Guéritte-Voegelein F, *et al.* A geranyl substituted flavonol from Macaranga vedeliana. *Phytochemistry* 1990 ; 29 : 2367–2368.

46. Mente NR, Wiemer AJ, Neighbors JD, *et al.* Total synthesis of (R,R,R)- and (S,S,S)-schweinfurthin F: Differences of bioactivity in the enantiomeric series. *Bioorg. Med. Chem. Lett.* 2007 ; 17 : 911–915.

47. Basabe P, Román M de, Diez D, *et al.* Synthesis of Isoprenyl Flavonoids: (+)-Denticulaflavonol, Macarangin, and Isomacarangin. *Synlett* 2008 ; 2008 : 1149–1152.

48. Comte G, Daskiewicz J-B, Bayet C, *et al.* C-Isoprenylation of Flavonoids Enhances Binding Affinity toward P-Glycoprotein and Modulation of Cancer Cell Chemoresistance. *J. Med. Chem.* 2001 ; 44 : 763–768.

49. Basabe P, Román M de, Marcos IS, *et al.* Prenylflavonoids and prenyl/alkyl-phloroacetophenones: synthesis and antitumour biological evaluation. *Eur. J. Med. Chem.* 2010 ; 45 : 4258–69.

50. Su F, Zhao Z, Ma S, *et al.* Cnidimonins A–C, Three Types of Hybrid Dimer from Cnidium monnieri: Structural Elucidation and Semisynthesis. *Org. Lett.* 2017 ; 19 : 4920–4923.

51. Quintin J, Lewin G. Regioselective 6-iodination of 5,7-dioxygenated flavones by benzyltrimethylammonium dichloroiodate. *Tetrahedron Lett.* 2004 ; 45 : 3635–3638.

52. Lu K, Chu J, Wang H, *et al.* Regioselective iodination of flavonoids by N-iodosuccinimide under neutral conditions. *Tetrahedron Lett.* 2013 ; 54 : 6345–6348.

53. Dutheuil G, Selander N, Szabó K, *et al.* Direct Synthesis of Functionalized Allylic Boronic Esters from Allylic Alcohols and Inexpensive Reagents and Catalysts. *Synthesis* 2008 ; 2008 : 2293–2297.

54. Höfener S, Kooijman PC, Groen J, *et al.* Fluorescence behavior of (selected) flavonols : a combined experimental and computational study. *Phys. Chem. Chem. Phys.* 2013 ; 15 : 12572–12581.

55. Duval R, Duplais C. Fluorescent natural products as probes and tracers in biology. *Nat. Prod. Rep.* 2017 ; 34 : 161–193.

56. Monago-Maraña O, Durán-Merás I, Galeano-Díaz T, *et al.* Fluorescence properties of flavonoid compounds. Quantification in paprika samples using spectrofluorimetry coupled to second order chemometric tools. *Food Chem.* 2016 ; 196 : 1058–1065.

57. Albulescu L, Strating JRPM, Thibaut HJ, *et al.* Broad-range inhibition of enterovirus replication by OSW-1, a natural compound targeting OSBP. *Antivir Res* 2015 ; 117 : 110–114.

58. Hancu G, Modroiu A., Chiral Switch: Between Therapeutical Benefit and Marketing Strategy. Pharmaceuticals 2022 ; 15,: 240.

59. Jezequel G, Rampal C, Guimard C *et al.* Structure-Based Design of a Lead Compound Derived from Natural Schweinfurthins with Antitumor Properties That Target Oxysterol-Binding Protein. J. Med. Chem. 2023 ; DOI: 10.1021/acs.jmedchem.3c01298

60. Oh-hashi K, Nakamura H, Ogawa H *et al.* Elucidation of OSW-1-Induced Stress Responses in Neuro2a Cells. Int. J. Mol. Sci. 2023 ; 24, 5787, doi.org/10.3390/ijms24065787

61. Du X, Turner N, Yang H. The Role of Oxysterol-Binding Protein and its Related Proteins in Cancer. *Semin Cell Dev Biol* 2018; 81: 149–153.

62. Roberts BL, Severance ZC, Bensen RC, *et al.* Differing Activities of Oxysterol-Binding Protein (OSBP) Targeting Antiviral Compounds. *Antivir Res* 2019 ; 170 : 104548.

63. Pierson TC, Diamond MS. The Continued Threat of Emerging Flaviviruses. *Nat Microbiol* 2020; 5 : 796–812.

64. De Palma AM, *et al.* Mutations in the Nonstructural Protein 3A Confer Resistance to the Novel Enterovirus Replication Inhibitor TTP-8307. *Antimicrob. Agents Chemother.* 2009; 53, 1850-1857.

65. Arita M *et al.* A bifunctional anti-enterovirus compound that inhibits replication and the early stage of enterovirus 71 infection. *J. Gen. Virol.* 2010; 91, 2734-2744

66. Gao Q et al. Discovery of Itraconazole with Broad-Spectrum In Vitro Antienterovirus Activity That Targets Nonstructural Protein 3A. *Antimicrob. Agents Chemother.* 2015; 59, 2654-2665.

67. Severance ZC *et al*. Structure−Activity Relationships of Ligand Binding to Oxysterol-Binding Protein (OSBP) and OSBP-Related Protein 4. J. Med. Chem. 2023; 66, 6, 3866–3875

68. Roberts BL *et al*. Differing activities of oxysterol-binding protein (OSBP) targeting anti-viral compounds. Antiviral Research 2019;170, No.104548

69. Pombo JP, Sanyal S. Perturbation of Intracellular Cholesterol and Fatty Acid Homeostasis During Flavivirus Infections. *Front. Immunol.* 2018 ; 9 : 1276.